Available online at www.sciencedirect.com
ScienceDirect
Lithos 103 (2008) 236–256
LITHOS
www.elsevier.com/locate/lithos

Transient hot channels: Perpetrating and regurgitating ultrahigh-pressure, high-temperature crust–mantle associations in collision belts

T.V. Gerya [a,*], L.L. Perchuk [b], J.-P. Burg [a]

[a] Department of Geosciences, Swiss Federal Institute of Technology - Zurich (ETH-Zurich), 8092 Zurich, Switzerland
[b] Department of Petrology, Moscow State University, 119899 Moscow, Russia

Received 20 March 2006; accepted 3 September 2007
Available online 3 October 2007

Abstract

Two-dimensional numerical modeling of early continental collision associated with subduction of the lithospheric mantle shows that the formation and exhumation of coesite- and diamond-bearing rocks metamorphosed at 700 to 900 °C in the presence of dense supercritical silicate fluids and melts may be explained by a transient "hot channel effect". Anomalously high temperature is caused by intense viscous and radiogenic heating in the channel composed of deeply subducted radiogenic upper-crustal rocks (especially, sediments of passive margin origin) and mantle rocks. Heating is associated with partial melting of crustal rocks caused by pervasive flow of aqueous fluids relieved by rapid dehydration (deserpentinization) of the overriding mantle lithosphere that has been hydrated during earlier subduction stages. The channel penetrates the plate interface to the bottom of the lithosphere of the overriding plate (150–200 km) and is characterized by metamorphic temperatures reaching 700 to 900 °C. Low effective viscosity of rocks subsequent to increased temperature, partial melting and fluid infiltration permits profound mixing of hydrated mantle and crustal rocks. The hot channel exists only during early collision, but rapidly produces large amounts of ultrahigh-pressure, high-temperature rocks. Further collision closes the channel by squeezing rheologically weak, partially molten, buoyant rocks between the strong lithospheric mantles of the two colliding plates. Assemblages of complicated P–T paths with repetitive loops characterize exhumation of ultrahigh-pressure rocks in the convoluted flow pattern of the hot channel.

Keywords: Exhumation of ultrahigh-pressure rocks; Continental collision; Subduction zones; Numerical modeling; Dehydration; Partial melting

1. Introduction

Studies of high-pressure (HP) and ultrahigh-pressure (UHP) metamorphic rocks exposed in collisional belts have shown that these units (1) are derived from both intermingled continental and oceanic crust, (2) are frequently associated with hydrated peridotite, (3) reveal a variable P–T–t record, with (4) narrow time constraints inferring that exhumation rates can be on the order of plate velocity (e.g. Perchuk et al., 1998; Amato et al., 1999; Rubatto and Hermann, 2001; Chopin, 2003; Liou and Zhang, 2004). The formation and exhumation of high- (HP) and ultrahigh-pressure (UHP) metamorphic complexes have been, since their discovery (Rosen et al., 1972; Chopin 1984), a puzzling problem (e.g. Schreyer, 1988; Ernst, 2001). Progresses

* Corresponding author. Fax: +41 44 6331065.
E-mail address: taras.gerya@erdw.ethz.ch (T.V. Gerya).

0024-4937/$ - see front matter © 2007 Elsevier B.V. All rights reserved.
doi:10.1016/j.lithos.2007.09.017

in numerical (Burov et al., 2001; Roselle and Engi, 2002; Gerya et al., 2002; Stöckhert and Gerya, 2005; Gerya and Stöckhert, 2006) and analog (e.g., Chemenda et al., 1995) modeling of geodynamic processes have identified several processes contributing to the formation and exhumation of (U)HP rocks, in particular those formed at relatively low peak metamorphic temperature (UHP–LT rocks <700 °C). The main processes are:

1) Forced return flow in a subduction/tectonic channel (e.g., Hsu, 1971; Cloos, 1982; Cloos and Shreve, 1988; Guinchi and Ricard, 1999; Roselle and Engi, 2002) reaching asthenospheric depths thanks to rheological softening of the overriding plate by water-bearing fluids released from the slab (Gerya et al., 2002, 2004a,b; Gerya and Stöckhert, 2006; Stöckhert and Gerya, 2005).
2) Multi-level circulation and forced ductile extrusion (squeezing) of rocks from a rheologically weak crustal channel (e.g., Burov et al., 2001).
3) Syn-collisional exhumation of large, coherent and buoyant crustal wedges (Chemenda et al., 1995) that can be accompanied by delamination of the crust and mantle layers of the subducting lithosphere (Boutelier et al., 2004).

The geodynamic significance of (ultra)high-pressure–high-temperature (UHP–HT) complexes (Fig. 1) remains more problematic (e.g. Bakun-Czubarow, 1998; Stöckhert et al., 2001, Tumiati et al., 2003; Stöckhert and Gerya, 2005; Gerya and Stöckhert, 2006). In many cases these complexes are composed of three major rock types — garnet peridotites, eclogites, and crustal metamorphic rocks (metabasites, metapelites, felsic gneisses etc; e.g., Obata and Morten, 1987; Bakun-Czubarow, 1991; Godard et al., 1996; O'Brien et al., 1997; Massonne, 1999; Klemd and Bröcker, 1999; Tumiati et al., 2003; Perchuk et al., 1995, 2004, 2005). Findings of ultrahigh-pressure (>6 GPa) mantle rocks (e.g., Dobrzhinetskaya et al., 1996; Roermund et al., 2000) in (U)HP–HT rock associations requires an understanding of crust–mantle mixing processes operating at asthenospheric depths and temperatures (e.g. Gerya et al., 2004a). Lastly, geochronology often suggests that UHP metamorphism takes place prior to collision (e.g., Eide and Liou 2000), a constraint that calls for attention to the transient period between subduction and collision.

From above considerations, we developed new high-resolution two-dimensional thermo-mechanical numerical models of subduction followed by continental collision in order to study the formation and exhumation of the (U)HP–HT complexes.

2. Numerical model

2.1. General setting

The 4000×670 km model (Fig. 2) is designed for the study of dynamic processes during continental collision associated with subduction of the lithospheric mantle (e.g., Burg and Gerya, 2005). A non-uniform 393×131 rectangular grid (Fig. 2a) with a resolution varying from 2 to 30 km provides the highest 2×2 km resolution in the upper central, 400 km wide and 100 km deep "orogenic" area of the model. We used ~7 million marker points to resolve details of model lithological structures (Fig. 2c). The model incorporates realistic rock rheology, partial melting process and viscous heating, which significantly influences metamorphic temperatures (Burg and Gerya, 2005).

The initial thermal structure of the lithosphere is laterally uniform with zero horizontal heat flow across the vertical boundaries (Fig. 2b) and corresponds to a usual continental geotherm (e.g. Turcotte and Schubert, 2002): 0 °C at the surface, 150 °C at 15 km depth, 400 °C at 35 km depth and 1300 °C at 142 km depth. The initial temperature gradient in the asthenospheric mantle is 0.5 °C/km. In the orogenic area of the model the lithospheric temperature profile is gradually bent

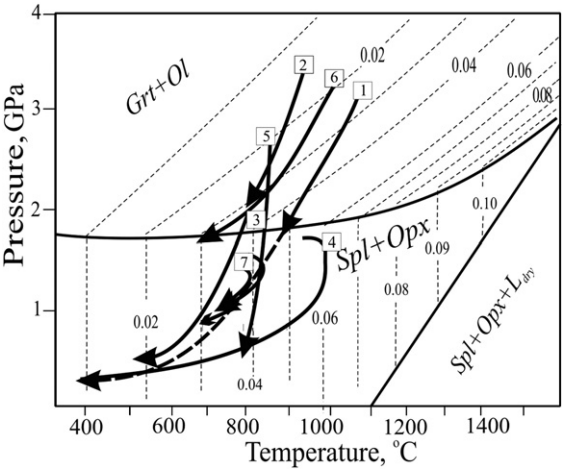

Fig. 1. Examples of *P–T* paths for (U)HP–HT complexes: 1 — garnet peridotites of Lower Austria (Carswell, 1991); 2 — diamondiferous gneiss of Central Erzgebirge (Massonne, 1999); 3 — felsic granulite of Central Erzgebirge (Willner et al., 1997); 4 — felsic granulite from Lower Austria (Carswell and O'Brien, 1993); 5 — Grt–Opx gneiss from southern Bohemia (Kotkova et al., 1997); 6 — felsic granulite from Snieznik, western Sudetes (Kryza et al., 1996). Peridotite solidus after Ito and Kennedy (1967); the reaction Ol+Grt=Opx+Spl curve after O'Hara et al. (1971). Dashed lines are isopleths of X_{Al}=Al/(Al+2 Mg+2Fe) in orthopyroxene. Abbreviations: Grt = garnet, Opx = orthopyroxene, Ol = olivine, Spl = spinel, L = melt.

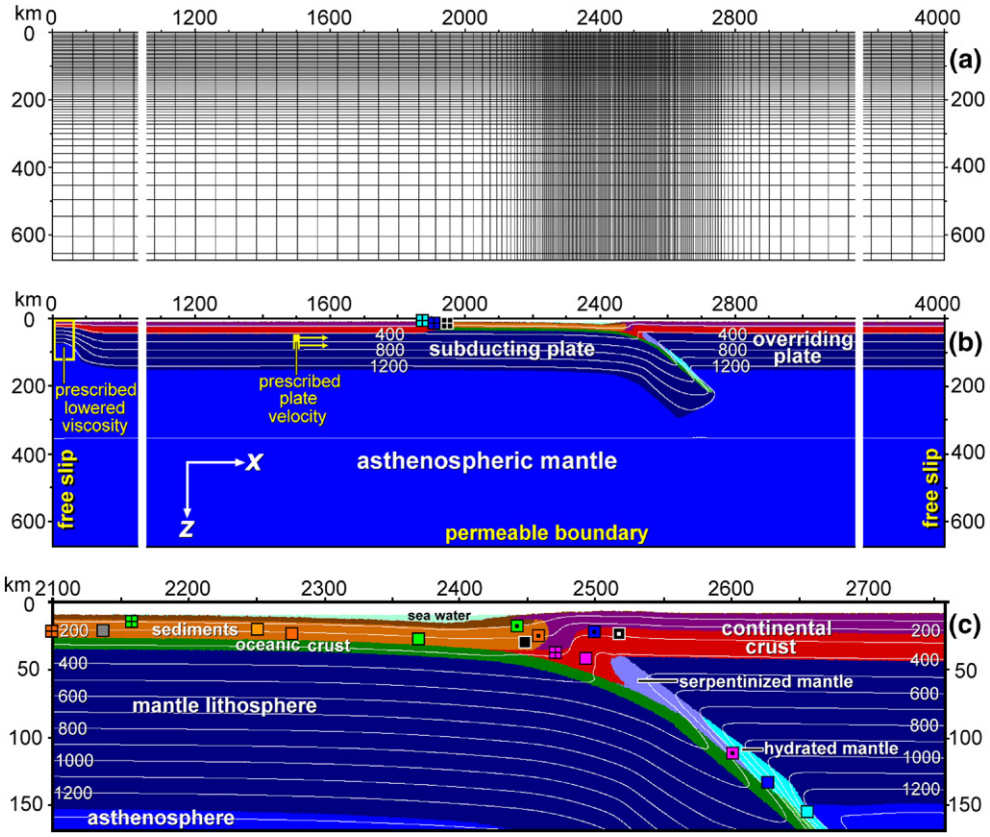

Fig. 2. 2-D numerical setting employed in this study: (a) geometry of non-uniform 393 × 131 rectangular numerical grid (only uneven horizontal and vertical lines of the grid are shown); (b) large-scale view of the entire model with temperature (isotherms in °C) and boundary conditions; (c) zoomed initial structure of subduction/collision zone. Different colors denote different lithologies (Table 2). The lithospheric and asthenospheric mantles have the same physical properties, different colors are used only for visualizing slab deformation and structural development. This is also the case for medium scale layering within the continental crust and sediments. Small colored squares in (b) and (c) show positions of representative markers (rock units) for which P–T paths are shown (Figs. 4, 7, 8, 9): open squares = Model 1 (Table 3, Fig. 4) and Model 16 (Table 3, Fig. 9); squares with dot = Model 9 (Table 3, Fig. 7); squares with cross = Model 15 (Table 3, Fig. 8). Different colors of these squares are used for discrimination of markers and do not correspond to the colors of rock types.

downward along the shape of the subducting slab (Fig. 2b). Infinite-like *external constant temperature conditions* along the lower boundary is implemented by using the following limitation: $\partial T/\partial z=(T_{\text{external}}-T)/\Delta z_{\text{external}}$, where $T_{\text{external}}=2045$ °C at 1670 km depth at the bottom external boundary, outside the model frame, and $\Delta z_{\text{external}}$ is the vertical distance from the lower boundary of the model to the external boundary where $T=T_{\text{external}}$ is satisfied (i.e. $\Delta z_{\text{external}}=1000$ km).

The velocity boundary conditions are free slip at all boundaries except the lower one, which is permeable in both downward and upward directions (Fig. 2b). Infinite-like *external free slip conditions* along the bottom imply free slip at 1670 km depth. Similarly to the usual free slip condition, external free slip allows global conservation of mass in the computational domain and is implemented by using the following limitation for velocity components at the lower boundary: $\partial v_x/\partial z=0$, $\partial v_z/\partial z=-v_z/\Delta z_{\text{external}}$, where $\Delta z_{\text{external}}$ is the vertical distance from the lower boundary of the model to the external boundary where free slip ($\partial v_x/\partial z=0$, $v_z=0$) is satisfied (i.e. $\Delta z_{\text{external}}=1000$ km). In order to minimize mechanical interaction of the cold slab with the permeable lower boundary, the maximal viscosity at 20 km deep region along this boundary was limited to 10^{21} Pa s.

Subduction/collision is prescribed by the rate of convergence (v_x) within the narrow *convergence condition domain* across the lithosphere (yellow arrows in Fig. 2b). The nucleation of the subduction/collision area is imposed by a 5–20 km wide and 150 km deep initially planar zone of hydrated mantle above a partly subducted oceanic slab that corresponds to the evolved stage of subduction under a continental margin (Gerya and Stöckhert, 2006). A

relatively large width of hydrated mantle above the slab is related to the significant amount of water released during subduction (e.g. Schmidt and Poli, 2001) and is consistent with results of numerical modelling concerning the spontaneously forming hydration zone (e.g., Gerya et al., 2002, 2006; Gerya and Stöckhert, 2006). Partial dehydration (deserpentinization) of the mantle releases large amounts of free water fluid with increasing temperature (e.g. Schmidt and Poli, 1998). This is visualized by changing mantle color when temperature rises above the serpentine stability field (cf. serpentinized and hydrated mantle in Fig. 2c). The 15 km thick pile of sediments on the 8 km thick oceanic crust simulates the transitional lithosphere structure at the passive margin coming in front of the overriding continental plate.

2.2. Topography

Incipient collision strongly affects the topographic evolution of adjacent regions. Models include surface movements in a simplified way. The surface is calculated dynamically at each time-step like a free surface by using the weak top layer approach (e.g. Gerya and Yuen, 2003b; Burg and Gerya, 2005). To model free surface and account for the topographic changes, we have implemented a low viscosity (10^{16}–10^{18} Pa s), initially 8 km thick layer above the upper continental crust (Fig. 2c). Its density is either 1 kg/m^3 (air, above $z=8$ km level) or 1000 kg/m^3 (sea water, below $z=8$ km level). The interface between this very weak layer and the top of the continental crust is treated as an erosion/sedimentation surface, which evolves according to the transport equation solved in Eulerian coordinates at each time-step (Gerya and Yuen, 2003b):

$$\partial z_{es}/\partial t = v_z - v_x \partial z_{es}/\partial x - v_s + v_e, \quad (1)$$

where z_{es} is the vertical position of the surface as a function of the horizontal distance x (cf. notations in Table 1); v_z and v_x are the vertical and horizontal components of the material velocity vector at the surface; v_s and v_e are sedimentation and erosion rates, respectively, which correspond to the relation:

$$v_s = 0\,\text{mm/a},\ v_e = v_{e0} \text{ when } z < 8\,\text{km},$$

$$v_s = v_{s0}\,\text{mm/a},\ v_e = 0 \text{ when } z > 8\,\text{km},$$

where v_{e0} and v_{s0} are imposed constant erosion and sedimentation rates, respectively. This simple erosion

Table 1
Abbreviations and units

Symbol	Meaning	Units
A_D	Material constant	$MPa^{-n}\cdot s^{-1}$
C	Cohesion	MPa
Cp	Isobaric heat capacity	$J\cdot K^{-1}\cdot kg^{-1}$
E	Activation energy	kJ mol^{-1}
G	Plastic potential	Pa
H_r, H_a, H_s	Radioactive, adiabatic and shear heat production	$W\cdot m^{-3}$
M	Volume fraction of melt	(Dimensionless)
n	Stress exponent	(Dimensionless)
P, P_{solid}	Dynamic pressure (mean stress on solids)	Pa
P_{fluid}	Pore fluid pressure	Pa
Q_L	Latent heat of melting	kJ kg^{-1}
t	Time	s
T	Temperature	K
$T_{liquidus}$, $T_{solidus}$	Liquidus and solidus temperature of a rock	K
V	Activation volume	$J\ MPa^{-1}\cdot mol^{-1}$
v_x, v_z	Horizontal and vertical components of velocity vector	$m\cdot s^{-1}$
x, z	Horizontal and vertical coordinates	m
Z	Viscoelasticity factor	(Dimensionless)
α	Thermal expansion coefficient	K^{-1}
β	Compressibility coefficient	Pa^{-1}
χ	Plastic multiplier	s^{-1}
$\dot{\varepsilon}_{ij}$	Components of the strain rate tensor	s^{-1}
η	Viscosity	Pa·s
λ	Pore fluid pressure coefficient: $\lambda=P_{fluid}/P_{solid}$	(Dimensionless)
μ	Shear modulus	Pa
ρ	Density	$kg\cdot m^{-3}$
σ_{II}	Second invariant of the deviatoric stress tensor	Pa
σ_{ij}	Components of the deviatoric stress tensor	Pa

model assumes both slope and elevation independent *large-scale erosion rate* (e.g. Vance et al., 2003) in a rapidly uplifting mountain belt.

2.3. Partial melting

Models allow melting of the continental crust and sediments in the P–T region between the wet solidus and dry liquidus of crustal rocks (Gerya and Yuen, 2003b). As a first approximation, the volumetric fraction of melt M is assumed to increase linearly with temperature according to the relations:

$$M = 0 \text{ at } T < T_{\text{solidus}}, \tag{2a}$$

$$M = (T - T_{\text{solidus}})/(T_{\text{liquidus}} - T_{\text{solidus}}) \text{ at } T_{\text{solidus}} < T < T_{\text{liquidus}}, \tag{2b}$$

$$M = 1 \text{ at } T > T_{\text{liquidus}}, \tag{2c}$$

T_{solidus} and T_{liquidus} are the wet solidus and dry liquidus temperatures of rock, respectively (Table 2).

The effective density, ρ_{eff}, of partially molten rocks is calculated from:

$$\rho_{\text{eff}} = \rho_{\text{solid}} - M(\rho_{\text{solid}} - \rho_{\text{molten}}), \tag{3}$$

where ρ_{solid} and ρ_{molten} are the densities of solid and molten rock, respectively, which vary with pressure and temperature according to the relation:

$$\rho_{P,T} = \rho_0[1 - \alpha(T - T_0)] \times [1 + \beta(P - P_0)], \tag{4}$$

where ρ_0 is the standard density at P_0=0.1 MPa and T_0=298 K; α and β are the thermal expansion and compressibility coefficients, respectively (Table 2).

The effects of latent heating are accounted for by an increased effective heat capacity (Cp_{eff}) and thermal expansion (α_{eff}) of the partially molten rocks ($0<M<1$), calculated as

$$Cp_{\text{eff}} = Cp + Q_{\text{L}}\left[(\partial M/\partial T)_P\right], \tag{5a}$$

$$\alpha_{\text{eff}} = \alpha + \rho Q_{\text{L}}\left[(\partial M/\partial P)_T\right]/T, \tag{5b}$$

where Cp and α are the heat capacity and the thermal expansion of the solid crust, respectively, and Q_{L} is the latent heat of melting of the crust (Table 2).

Table 2
Material properties[a] used in 2-D numerical experiments

Material	ρ_0, kg/m^3	k, W/(m K)	T_{solidus}, K	T_{liquidus}, K	Q_{L}, kJ/kg	H_{r}, μW/m^3	Flow law	E, kJ/mol	n	A_{D}, MPa^{-n}·s^{-1}	V, J/(MPa·mol)	μ, GPa
Continental crust, sediments	2700 (solid)	[0.64+807/(T+77)]×exp(0.00004P_{MPa})	889+17,900/(P+54)+20,200/(P+54)^2 at P<1200 MPa, 831+0.06P at P>1200 MPa	1262+0.09P	300	0.5–5	Wet quartzite	154	2.3	$10^{-3.5}$	0	10
	2400 (molten)											
Oceanic crust	3000–3500 (solid)	[1.18+474/(T_{K}+77]×exp(0.00004P_{MPa})	973–70,400/(P+354)+77,800,000/(P+354)^2 at P<1600 MPa, 935+0.0035P+0.0000062P^2 at P>1600 MPa	1423+0.105P	380	0.25	Plagioclase An_{75}	238	3.2	$10^{-3.5}$	0	25
	2900 (molten)											
Lithosphere–asthenosphere dry mantle	3300	[0.73+1293/(T_{K}+77]×exp(0.00004P_{MPa})	–	–	–	0.022	Dry olivine	532	3.5	$10^{4.4}$	8	67
Hydrated mantle in subduction shear zone	3000–3300	[0.73+1293/(T_{K}+77]×exp(0.00004P_{MPa})	–	–	–	0.022	Wet olivine,	470	4	$10^{3.3}$	8	67
References[b]	1, 2	3	4	4	1, 2	1	5	5	5	5	1, 5	1

[a] Cp=1000 J kg^{-1}K^{-1}, $\alpha=3\times10^{-5}$ K^{-1}, $\beta=1\times10^{-5}$ MPa^{-1} for all rock types.
[b] 1 = (Turcotte and Schubert, 1982); 2 = (Bittner and Schmeling, 1995); 3 = (Clauser and Huenges, 1995); 4 = (Schmidt and Poli, 1998); 5 = (Ranalli, 1995).

2.4. Rheological model

We employed a viscoelastoplastic rheology with the bulk strain rate $\dot{\varepsilon}_{ij}$ including three respective components:

$$\dot{\varepsilon}_{ij} = \dot{\varepsilon}_{ij(\text{viscous})} + \dot{\varepsilon}_{ij(\text{elastic})} + \dot{\varepsilon}_{ij(\text{plastic})}, \quad (6)$$

where

$$\dot{\varepsilon}_{ij(\text{viscous})} = \frac{1}{2\eta}\sigma_{ij},$$

$$\dot{\varepsilon}_{ij(\text{elastic})} = \frac{1}{2\mu}\frac{D\sigma_{ij}}{Dt},$$

$$\dot{\varepsilon}_{ij(\text{plastic})} = 0 \text{ when } \sigma_{\text{II}} < \sigma_{\text{yield}} \text{ and } \dot{\varepsilon}_{ij(\text{plastic})} = \chi\frac{\partial G}{\partial \sigma_{ij}} = \chi\frac{\sigma_{ij}}{2\sigma_{\text{II}}} \text{ when } \sigma_{\text{II}} = \sigma_{\text{yield}},$$

$$\sigma_{\text{II}} = \left(1/2\sigma_{ij}\sigma_{ij}\right)^{1/2},$$

$$G = \sigma_{\text{II}},$$

where $\frac{D\sigma_{ij}}{Dt}$ is objective co-rotational time derivative of deviatoric stress component σ_{ij}, σ_{yield} is plastic yield strength for given rock, σ_{II} is second deviatoric stress invariant, G is plastic potential (cf. discussion in Gerya and Yuen, 2007) and χ is plastic multiplier satisfying plastic yielding condition $\sigma_{\text{II}}=\sigma_{\text{yield}}$. In majority of numerical experiments simplified viscoplastic rheology has been used implying a zero elastic strain rate component.

The viscosity of solid rocks ($M \leq 0.1$) essentially depends on stress, pressure and temperature. It is defined in terms of second deviatoric stress invariant σ_{II} (Ranalli, 1995) as:

$$\eta = \left(\frac{4}{\sigma_{\text{II}}}\right)^{(n-1)}\frac{F^n}{A_{\text{D}}}\exp\left(\frac{E+V}{RT}\right), \quad (7)$$

where A_{D}, E, V and n are experimentally determined flow law parameters (Table 2). F is a dimensionless coefficient depending on the type of experiments on which the flow law is based (Ranalli, 1995). For example:

$$F = \frac{2^{(1-n)/n}}{3^{(1+n)/2n}} \text{ for triaxial compression and}$$

$$F = 2^{(1-2n)/n} \text{ for simple shear.}$$

Partially molten rocks ($M > 0.1$) are assigned a reduced effective viscosity of 10^{17} Pa·s which equals the upper bound for partially molten systems (10^{14}–10^{17} Pa·s, e.g., Pinkerton and Stevenson, 1992) but still is much lower than the effective viscosity of solid rocks (10^{18}–10^{26} Pa·s). 10^{16} and 10^{26} Pa s are the lower and upper viscosity cut values for all types of model materials.

The plastic yield strength of rocks under fluid-present conditions strongly depends on the ratio between solid (P_{solid}) and fluid (P_{fluid}) pressure according to (Ranalli, 1995; Brace and Kohlestedt, 1980):

$$\sigma_{\text{yield}} = C + (N_1 P + N_2)(1-\lambda), \quad (8)$$

where C is the cohesion (residual strength at $P=0$), $\lambda = \frac{P_{\text{fluid}}}{P_{\text{solid}}}$ is the pore fluid pressure factor, $P_{\text{solid}}=P$ corresponds to mean stress on solids (i.e., dynamic non-lithostatic solid pressure), N_1 and N_2 are empirical constants defined experimentally (Brace and Kohlestedt, 1980) for dry fractured crystalline rocks ($N_1=0.85$, $N_2=0$ when $P<200$ MPa and $N_1=0.6$, $N_2=60$ MPa when $P>200$ MPa).

The pore fluid pressure factor λ controls the brittle strength of fluid-containing porous or fractured media. A hydrostatic gradient with a pore pressure coefficient $\lambda=0.4$ is generally accepted for the upper crust (e.g. Sibson, 1990). Hydrocarbon exploration wells have shown that in sedimentary basins the transition from a hydrostatic to a near-lithostatic pore pressure gradient generally occurs at about 3 to 5 m depth (e.g. Sibson, 1990). However, the KTB and Kola boreholes have shown that a hydrostatic pore pressure gradient can reach down to more then 9 km depth and a temperature of 265 °C (Grawinkel and Stöckhert, 1997; Huenges et al., 1997; Kukkonen and Clauser, 1994). For simplicity, we assumed a continuous transition from the hydrostatic pore fluid pressure ($\lambda=0.4$) at the surface to a characteristic pore fluid pressure ($\lambda_{10}=0.75$–0.9) at 10 km depth. Intermediate pore fluid pressures are thus assumed at shallow depths <10 km, with an effective pore fluid pressure calculated as follows (Gerya et al., 2002):

$$\lambda = \frac{0.4(10-\Delta z_{\text{es}}) + \lambda_{10}\Delta z_{\text{es}}}{10} \text{ when } 0 \leq \Delta z_{\text{es}} \leq 10\,\text{km} \quad (9)$$

$$\lambda = \lambda_{10} \text{ when } \Delta z_{\text{es}} > 10\,\text{km},$$

where Δz_{es} is the depth beneath the calculated dynamic erosion/sedimentation surface in km. The brittle strength of the mantle is assumed to be high because of the absence of free pore fluid ($\lambda_{10}=0$ in Eq. 9).

2.5. Conservation equations and numerical implementation

We have considered 2-D creeping flow wherein both thermal and chemical buoyant forces are included along with heating from adiabatic compression and viscous dissipation in the heat conservation equation.

We have adopted a Lagrangian frame (Gerya and Yuen, 2003a) in which the heat conservation equation with thermal conductivity $k(T,P,c)$ (Table 2) depending on rock composition (c), pressure and temperature takes the form:

$$\rho Cp\left(\frac{DT}{Dt}\right) = -\frac{\partial q_x}{\partial x} - \frac{\partial q_z}{\partial z} + H_r + H_a + H_S \qquad (10)$$

$$q_x = -k(T,P,c)\frac{\partial T}{\partial x} \quad q_z = -k(T,P,c)\frac{\partial T}{\partial z},$$

$$H_a = T\alpha\left(v_x\frac{\partial P}{\partial x} + v_z\frac{\partial P}{\partial z}\right)$$

$$H_S = \sigma_{xx}\left(\dot{\varepsilon}_{xx} - \dot{\varepsilon}_{xx(\text{elastic})}\right) + \sigma_{zz}\left(\dot{\varepsilon}_{zz} - \dot{\varepsilon}_{zz(\text{elastic})}\right) + 2\sigma_{xz}\left(\dot{\varepsilon}_{xz} - \dot{\varepsilon}_{xz(\text{elastic})}\right),$$

where D/Dt represents the substantive time derivative, H_r is the radioactive heating that depends on rock composition (Table 2) and other notations are shown in Table 1.

The conservation of mass is approximated by the incompressible mass conservation (continuity) equation (e.g. Turcotte and Schubert, 2002).

$$\frac{\partial v_x}{\partial x} + \frac{\partial v_z}{\partial z} = 0. \qquad (11)$$

The 2-D Stokes equations for creeping flow take the form:

$$\frac{\partial \sigma_{xx}}{\partial x} + \frac{\partial \sigma_{xz}}{\partial z} = \frac{\partial P}{\partial x} \qquad (12)$$

$$\frac{\partial \sigma_{zz}}{\partial z} + \frac{\partial \sigma_{xz}}{\partial x} = \frac{\partial P}{\partial z} - g\rho(T,P,c,M). \qquad (13)$$

The density $\rho(T,P,c,M)$ depends explicitly on temperature, pressure, rock composition and melt fraction. Deviatoric stress components σ_{ij} in Eqs. (12), (13) are formulated from viscoelastoplastic constitutive relationships (Eq. 14) by using first order finite-differences in time $\frac{D\sigma_{ij}}{Dt} = \frac{\sigma_{ij}-\sigma_{ij}^o}{\Delta t}$ for representing time derivatives of elastic stresses (e.g. Moresi et al., 2003)

$$\sigma_{ij} = 2\eta_{vp}\dot{\varepsilon}_{ij}Z + \sigma_{ij}^o(1-Z), \qquad (14)$$

$$Z = \frac{\Delta t\mu}{\Delta t\mu + \eta_{vp}},$$

$$\eta_{vp} = \eta \text{ when } \sigma_{II} < \sigma_{\text{yield}} \text{ and } \eta_{vp} = \eta\frac{\sigma_{II}}{\eta\chi + \sigma_{II}} \text{ when } \sigma_{II} = \sigma_{\text{yield}},$$

in which Δt is elastic time-step, σ_{ij}^o is deviatoric stress components from the previous time slice corrected for advection and rotation by using non-diffusive marker-in-cell technique (e.g. Moresi et al., 2003; Gerya and Yuen, 2003a). Z is the viscoelasticity factor and η_{vp} is a viscosity-like parameter computed iteratively to satisfy plastic yielding condition ($\eta_{vp}=\eta$ when no plastic yielding occur). It is worth noting that dynamic (and not depth-dependent lithostatic) pressure was consistently used in all calculations including rheological and melting models, thus taking into account effects of non-lithostatic pressures in deforming regions (Petrini and Podladchikov, 2000; Burg and Gerya, 2005; Buiter et al., 2006). We employed the 2-D code I2ELVIS (Gerya and Yuen, 2003a; Gerya and Yuen, 2007) based on finite-differences with a non-diffusive marker-in-cell technique used for advecting and updating material properties such as rock type, temperature, stress and plastic strain. The code allows for the accurate conservative solution of the governing equations on a rectangular fully staggered Eulerian grid. The code was tested for a variety of problems by comparing results with both analytical solutions (Gerya and Yuen, 2003a; Gerya and Yuen, 2007) and analogue sandbox experiments (Buiter et al., 2006).

3. Results

Figs. 3, 4 and 5 summarize the results of the typical Model 1 (Table 3). Incipient collision between the two continental plates associated with subduction of the mantle lithosphere (Fig. 3) leads to the formation of a deep planar channel (cf. Engi et al., 2001) involving crustal rocks (mainly sediments) and hydrated mantle. This channel penetrates down to some 150 km depth, i.e. to the bottom of the overriding lithosphere (Fig. 4, 7.0 Myr). The stability of this channel is due to the

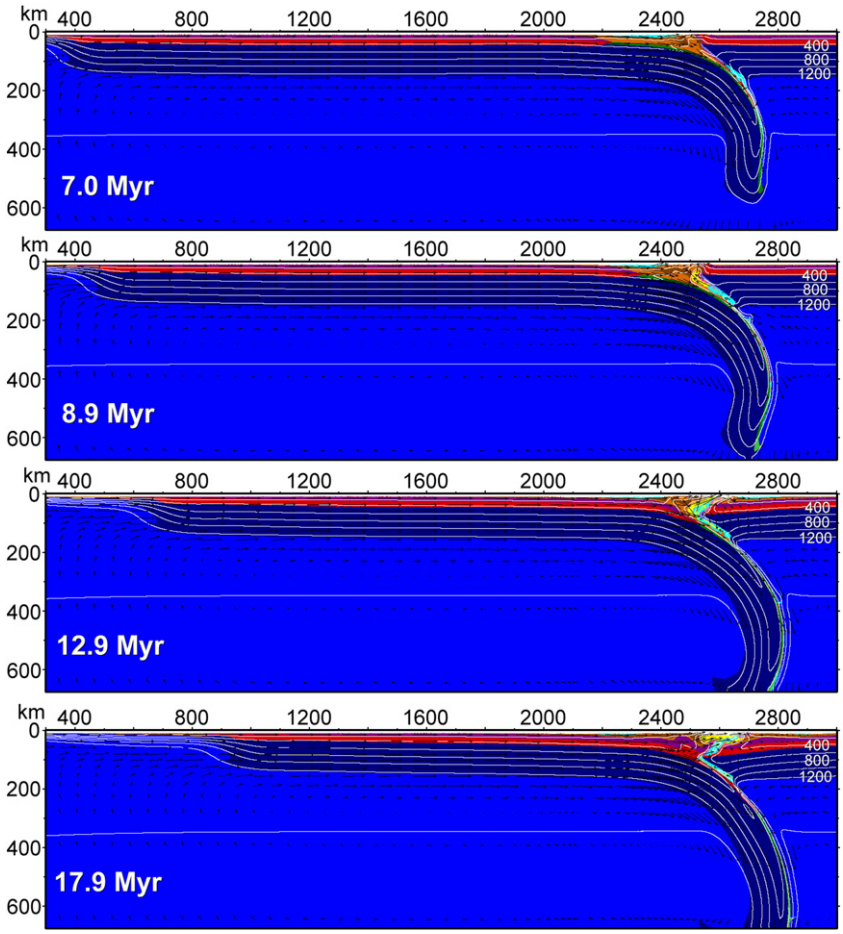

Fig. 3. Large-scale development of reference Model 1, with convergence rate = 5 cm yr^{-1} (Table 3). Time (Myr) of shortening is given in the figures. White numbered lines are isotherms in °C. Arrows show the calculated velocity field. High strength of the cold deeply subducted mantle lithosphere prevents its unbending and causes strong slab curvature.

mechanical equilibrium between subduction drag and bulk positive buoyancy of channel rocks, namely subducted sediments and serpentinized mantle formed during the preceding subduction stages (Gerya et al., 2002; Gerya and Stöckhert, 2006). The weak rheological properties of these rocks lower the channel effective viscosity (Fig. 5a), which provides favorable conditions for the onset of return flow (Gerya et al., 2002; Gerya and Stöckhert, 2006) and mechanical mixing of subducted rocks with hydrated mantle of the hanging wall, above the slab (Fig. 4, 8.9 Myr). Temperature rapidly increases within the tectonic channel (Fig. 4, 7.0–8.9 Myr) due to intense internal heat production from combined viscous heating (Fig. 5b) and radioactivity (Table 3) of subducted sediments (Burg and Gerya, 2005). Viscous heating in the channel is caused by the resistance of buoyant rocks to subduction drag. This heating can reach several tens of $\mu W/m^3$ (i.e. one order of magnitude higher than radioactive heating) and is strongest along both upper and lower channel boundaries (Fig. 5b). The channel thus becomes thermally isolated from both subducting and overriding plates, which allows its internal temperature to rise rapidly up to 700–900 °C. At these temperatures, subducted crustal rocks melt under UHP conditions (Fig. 4, 8.9 Myr). The increased temperature also causes breakdown of serpentine in the hydrated mantle (c.f. displacement of serpentinized mantle boundary in the channel in Fig. 4, 7.0–8.9 Myr) formed during subduction (e.g., Peacock, 1987; Schmidt and Poli, 1998; Gerya et al., 2002; Gerya and Stöckhert, 2006). Mantle dehydration implies liberation of a large amount of aqueous fluids in the channel, which further enhance melting of mixed crustal and mantle rocks. Intensity of crust/mantle mixing in the channel is variable (Table 3) and mainly depends on rheology of hydrated mantle rocks. Maximal degree of mixing (Fig. 4) is achieved in numerical experiments exploring low constant (10^{19} Pa s) viscosity of hydrated mantle (cf.

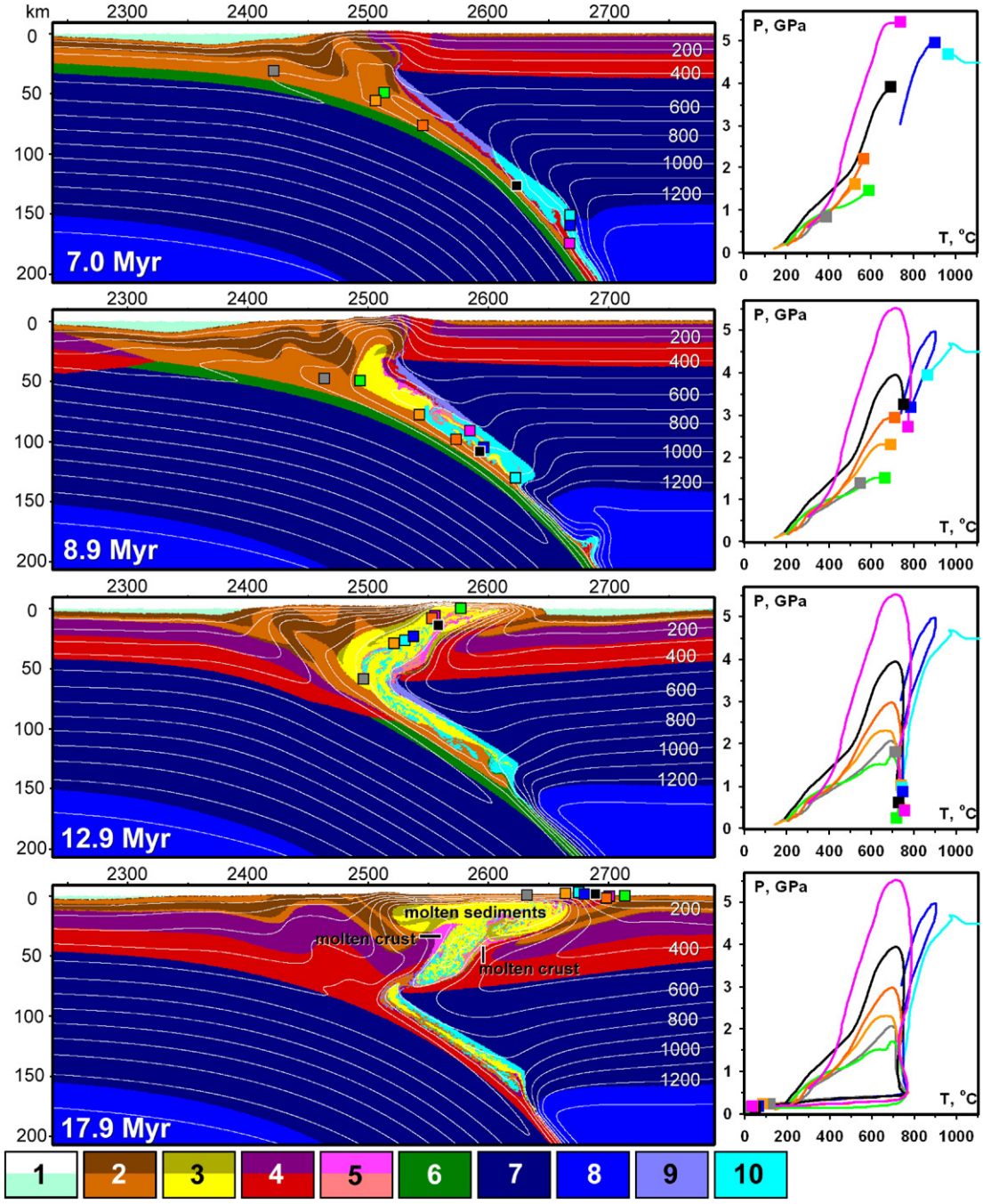

Fig. 4. Enlarged 550×210 km areas of the original 4000 km×670 km reference Model 1, with convergence rate=5 cm yr^{-1} (Table 3). Color code: 1 = weak layer (air, water); 2,3 = sediments (2 — solid, 3 — partially molten); 4,5 = continental crust (4 — solid, 5 — partially molten); 6 = oceanic crust; 7 = mantle lithosphere; 8 = asthenospheric mantle; 9 = serpentinized mantle; 10 = hydrated serpentine-free mantle. Time (Myr) of shortening is given in the figures. White numbered lines are isotherms in °C. Small colored squares show positions of representative markers (rock units) for which *P–T* paths are shown. Initial positions of markers are shown in Fig. 2. Colors of these squares are used for discrimination of marker points plotted in *P–T* diagrams and do not correspond to the colors of rock types. Vertical scale: depth below the $z=8$ km sea level.

discussion in Gerya et al., 2002). Increase in buoyancy due to melting destabilizes the channel that starts to extrude upwards (Fig. 4, 8.9–12.9 Myr). Exhumation associated with vigorous internal deformation causes further mixing of crustal and mantle rocks (Fig. 4, 8.9–12.9 Myr). Rapid decompression (Fig. 6b, d) further

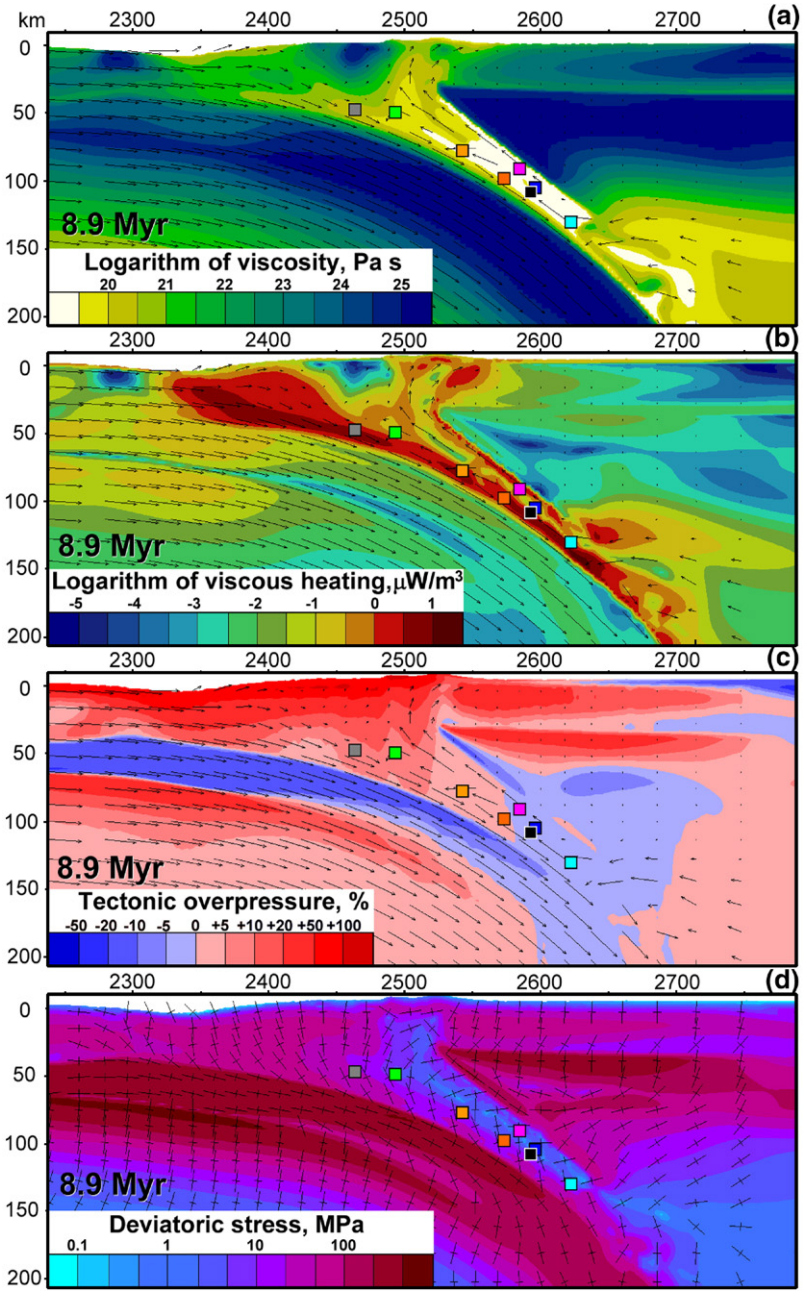

Fig. 5. Enlarged 550×210 km area of the original 4000 km×670 km reference Model 1 (Figs. 3, 4; Table 3) at 8.9 Myr after beginning of shortening: (a) — viscosity field (Pa s), (b) — viscous heating (10^{-6} W/m^3), (c) — distributions of the non-lithostatic pressure component $\Delta P = 100(P - P_{lith})/P_{lith}$, (d) — stress field (second invariant of deviatoric stress tensor $\sigma_{II} = (1/2\sigma_{ij}\sigma_{ij})^{1/2}$). Arrows in (a), (b) and (c) show the calculated velocity field. Long and short branches of elongated crosses in (d) show orientations of largest (extension direction) and smallest (shortening direction) principal stress axes, respectively.

enhances melting and produces large volumes of partially molten rocks emplaced in the middle–upper crust (Fig. 4, 17.9 Myr). Strong lateral metamorphic zoning characterizes this stage (c.f. distribution of representative P–T–time paths in Fig. 4, 17.9 Myr). Massive UHP rock extrusion generates dramatic thinning and ultimately closure of the tectonic channel (Fig. 4, 17.9 Myr) once the two continents meet (cf. convergence of red/magenta continental crust segments in Fig. 4, 8.9–17.9 Myr). The existence of the hot tectonic channel is thus limited to the few Myr transition from subduction to collision.

Table 3
Parameters[a] of selected numerical experiments

Model	Upper continental crust		Lower continental crust		Sediments		Oceanic crust		Hydrated serpentine-free mantle[a]		Hydrated serpentine bearing mantle		v_{e0}, mm/a	v_{s0}, mm/a	Convergence rate, cm/a	Shear heating	Hot channel	Tectonic underplating	Slab delamination	Crust–mantle mixing
	λ_{10}	H_r, μW/m^3	λ_{10}	H_r, μW/m^3	λ_{10}	H_r, μW/m^3	λ_{10}	ρ_0, kg/m^3	λ_{10}	ρ_0, kg/m^3	λ_{10}	ρ_0, kg/m^3								
1 (chaa)	0.75	2	0.75	0.5	0.75	5	0.90	3300	1[b]	3200	1[b]	3000	3	1	5	+	+	nucl.[c]	nucl.	Strong
2 (chad)	0.75	2	0.75	0.5	0.75	2	0.90	3300	1[b]	3200	1[b]	3000	3	1	5	+	+	nucl.	+	Strong
3 (chag)	0.75	2	0.75	0.5	0.75	2	0.90	3300	1[b]	3200	1[b]	3000	1	1	3	+	+	−	+	Strong
4 (chah)	0.75	2	0.75	0.5	0.75	2	0.90	3300	1[b]	3200	1[b]	3000	1	1	10	+	+	−	nucl.	Strong
5 (chai)	0.75	2	0.75	0.5	0.75	2	0.90	3300	0.90	3200	0.90	3000	1	1	5	+	+	−	nucl.	Weak
6 (chaj)	0.75	2	0.75	0.5	0.75	2	0.90	3000	0.90	3200	0.90	3000	1	1	5	+	+	−	+	Weak
7 (chak)	0.75	2	0.75	0.5	0.75	2	0.90	3500	0.90	3200	0.90	3000	1	1	5	+	+	−	+	Weak
8 (chal)	0.75	2	0.75	0.5	0.75	2	0.90	3300	0.98	3200	0.98	3000	1	1	5	+	+	−	+	Weak
9 (cham)	0.75	2	0.75	0.5	0.75	2	0.90	3300	1[b]	3200	1[b]	3000	1	1	5	−	−	+	−	−
10 (chan)	0.75	2	0.75	0.5	0.75	4	0.90	3300	0.98	3200	0.98	3000	1	1	5	+	+	nucl.	+	Medium
11 (chao)	0.75	2	0.75	0.5	0.75	4	0.90	3300	0.98	3200	0.98	3000	1	1	5	−	+	+	+	Weak
12 (chbb)[d]	0.75	2	0.75	0.5	0.75	5	0.90	3300	1[b]	3200	1[b]	3300	3	1	5	+	nucl.	−	−	Strong
13 (chbc)[d]	0.75–0.92[e]	2	0.75–0.92[e]	0.5	0.75–0.92[e]	2	0.75–0.92[e]	3300	0.98	3200	0.98	3300	3	1	5	+	+	+	+	Weak
14 (chbe)[d]	0.75	2	0.75	0.5	0.75	2	0.75	3300	0.98	3200	0.98	3300	3	1	5	+	+	+	+	Weak
15 (chbf)[d]	0.75	2	0.75	0.5	0.75	2	0.90	3300	0.98	3200	0.98	3000	3	1	5	+	+	+	+	Weak
16 (chap)	0.75	2	0.75	0.5	0.75	5	0.90	3300	1[b]	3200	1[b]	3000	0	1	5	+	+	nucl.	+	Strong

[a] Hydrated mantle beyond the serpentine stability field (Schmidt and Poli, 1998), $T>751+0.18P-0.000031P^2$ at $P<2100$ MPa, $T>1013-0.0018P-0.0000039P^2$ at $P>2100$ MPa.
[b] Constant lowered viscosity 10^{19} Pa s (Gerya et al., 2002) was adopted for the hydrated mantle.
[c] Nucleation of the feature.
[d] Viscoelastoplastic rheology is used.
[e] Linear increase of λ_{10} from 0.75 to 0.92 for plastic strain from 0.5 to 1.5 is applied for all crustal rocks implying pore fluid pressure increase during plastic deformation.

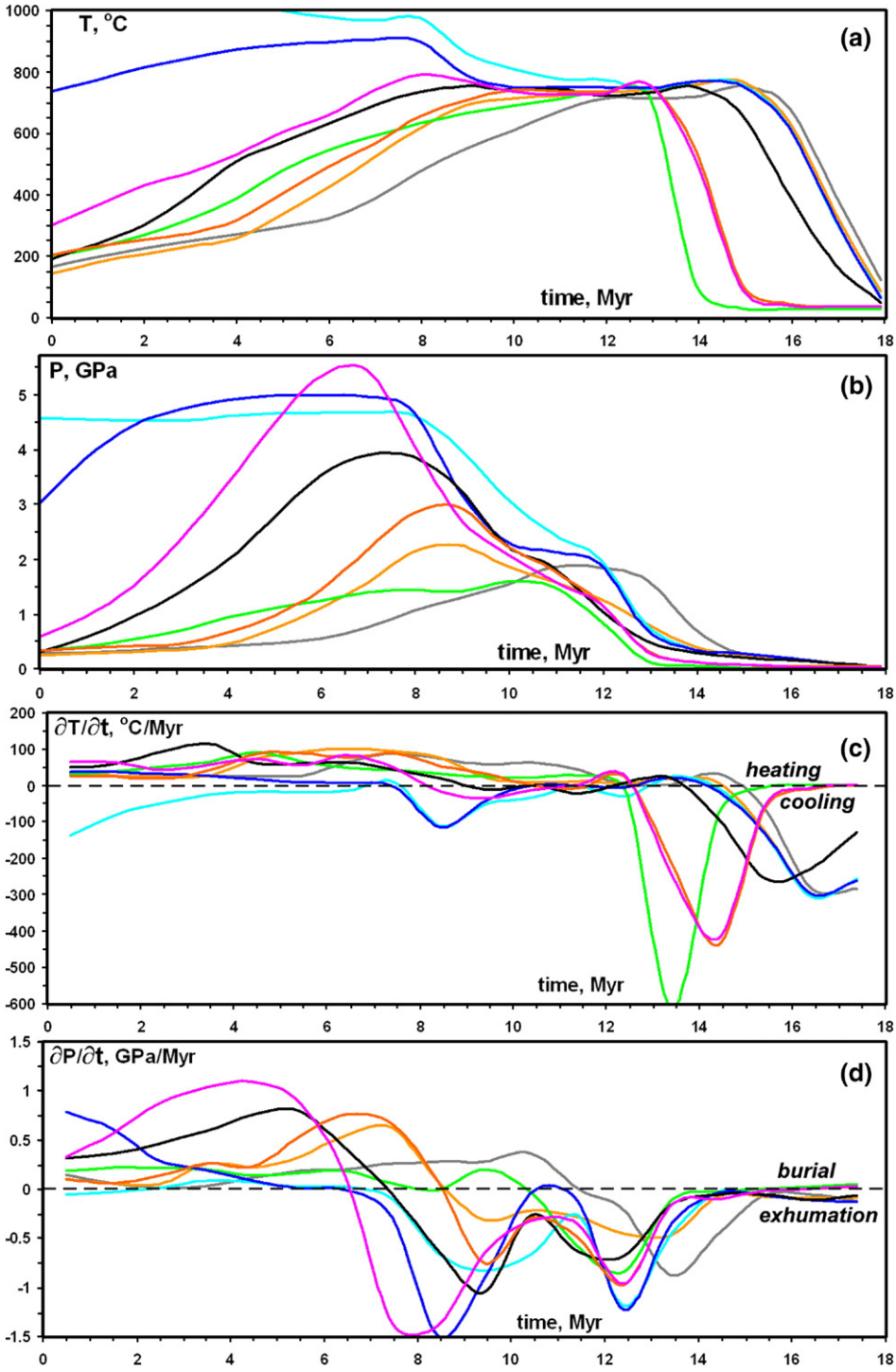

Fig. 6. Evolution of temperature (a), pressure (b), heating/cooling rate (c) and pressurizing/decompression rate (d) for representative markers (rock units) of Model 1 (Figs. 4, 5, Table 3). Positions and P–T paths of the markers are shown in Fig. 4.

The establishment of hot channel tectonics crucially depends on the intensity of internal heating. Numerical experiments without viscous heating and/or lower radiogenic heat production evolve into different transient processes such as tectonic underplating of subducted crustal rocks beneath the overriding lithosphere (Figs. 7, 8), a process also produced in analog experiments (Chemenda et al., 2000; Boutelier et al., 2004). In the

numerical case, mixed crustal and hydrated mantle rocks extrude from the deep tip of the channel in form of chemical plume, which is colder but yet positively buoyant compared to the asthenospheric mantle (Fig. 7, 13.0–18.0 Myr). Lateral spreading of the relatively cold plume into the hot (>1000 °C) mantle gradually heats up subducted rocks above 1000 °C, which leads to melting at pressures of 4–5 GPa (i.e., under UHP–UHT conditions, Fig. 7, 13.0–18.0 Myr, Fig. 8, 15.8–26.8 Myr). The development of similar structures called "mixed cold plumes" has been studied for both oceanic and continental margin subduction and have strong implications for the

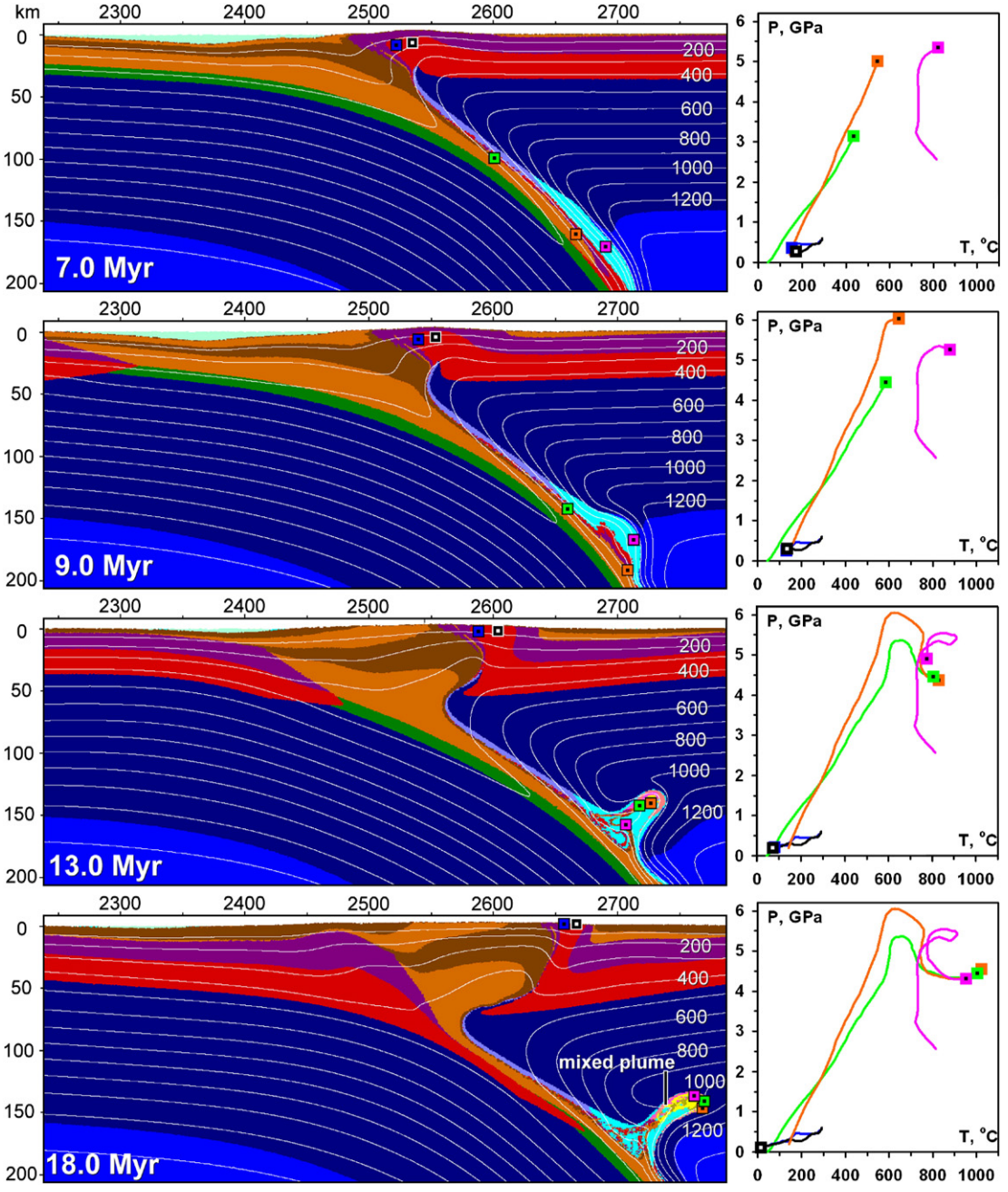

Fig. 7. Enlarged 550×210 km areas of the original 4000 km×670 km reference Model 9, with convergence rate=5 cm yr^{-1} (Table 3). No viscous heating is included for this model. Rock colors are as in Fig. 4. Time (Myr) of shortening is given in the figures. White numbered lines are isotherms in °C. Colored squares show positions of representative markers (rock units) for which *P*–*T* paths are shown. Initial positions of markers are shown in Fig. 2. As in Fig. 4, marker colors do not correspond to that of rock types. Vertical scale: depth below the $z=8$ km sea level.

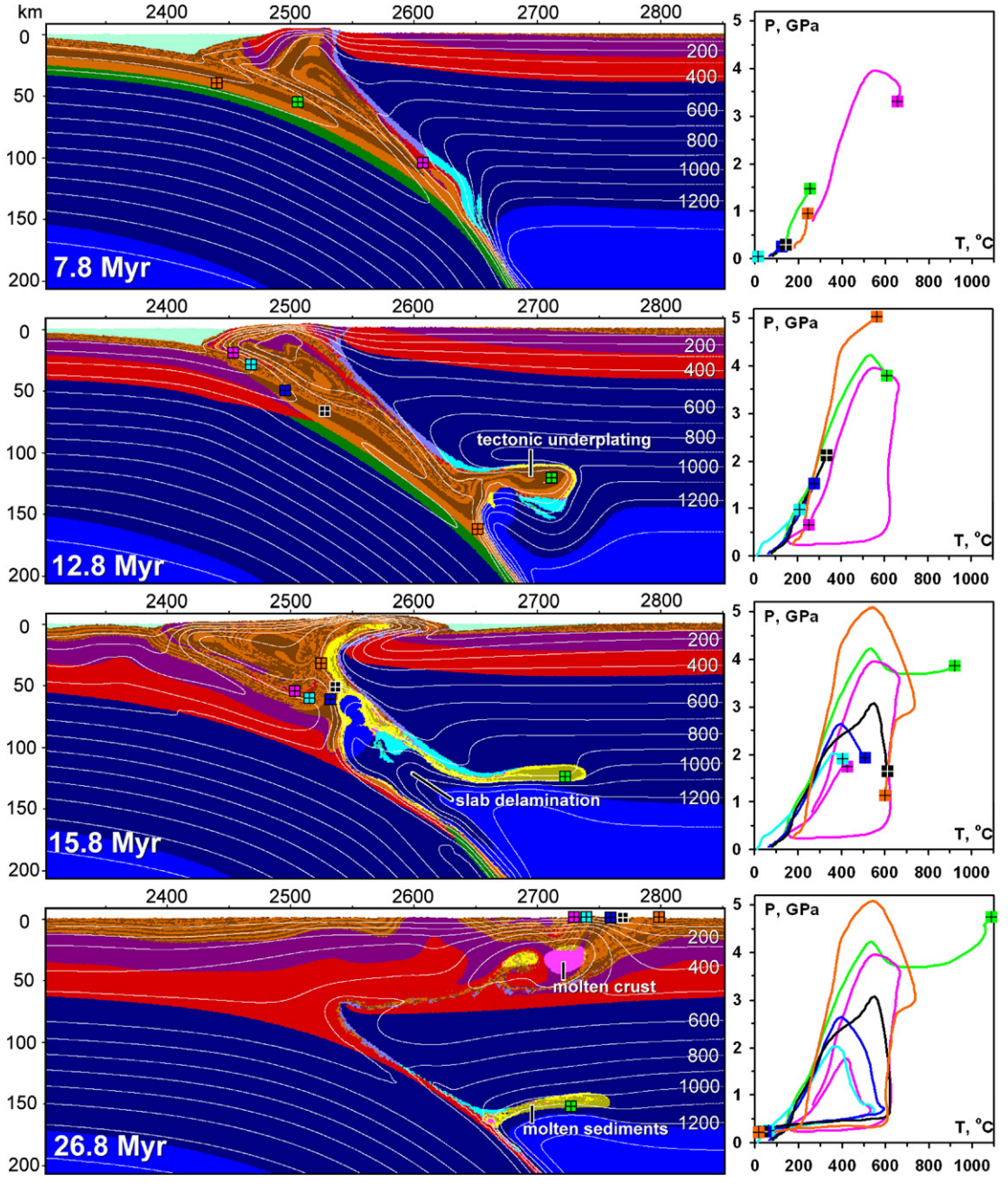

Fig. 8. Enlarged 550×210 km areas of the original 4000 km×670 km reference Model 15, with convergence rate=5 cm yr^{-1} (Table 3). Rock colors are as in Fig. 4. Time (Myr) of shortening is given in the figures. White numbered lines are isotherms in °C. Colored rectangles show positions of representative markers (rock units) for which *P*–*T* paths are shown. Initial positions of markers are shown in Fig. 2. As in Fig. 4, marker colors do not correspond to that of rock types. Vertical scale: depth below the z=8 km sea level.

magmatic activity in volcanic arcs (Gerya and Yuen, 2003b; Gerya and Stöckhert, 2006; Gerya et al., 2006).

Tectonic underplating is generally not associated with exhumation of UHP rocks and produces metamorphic zoning of low pressure (0.4–0.6 GPa) — low temperature (300–400 °C) conditions (Fig. 7, 18.0 Myr). Therefore, the hot channel (Fig. 4) and underplated cold plumes (Fig. 7) are alternative end-members of the incipient collision process. Mixed types of models are commonly generated in numerical experiments (Table 3; Fig. 8, also cf. nucleation of cold plume in Fig. 4, 8.9 Myr).

Fig. 8 shows that extrusion of the hot channel may be coupled with slab delamination (Fig. 8, 15.8 Myr; Table 3), which triggers underplating of the extruding channel material. Then, the rising hot asthenospheric mantle enhances melting of crustal rocks along the decompression P–T path (Fig. 8, 15.8 Myr). Subsequent convergence closes the space between the two plates, hence creating a geometry typical of mature collision with a shallow wedge-like channel closed from below (Fig. 8, 26.8 Myr; Burg and Gerya, 2005). At this stage, a large volume of crustal material tectonically emplaced below the lithosphere flattens and becomes molten under

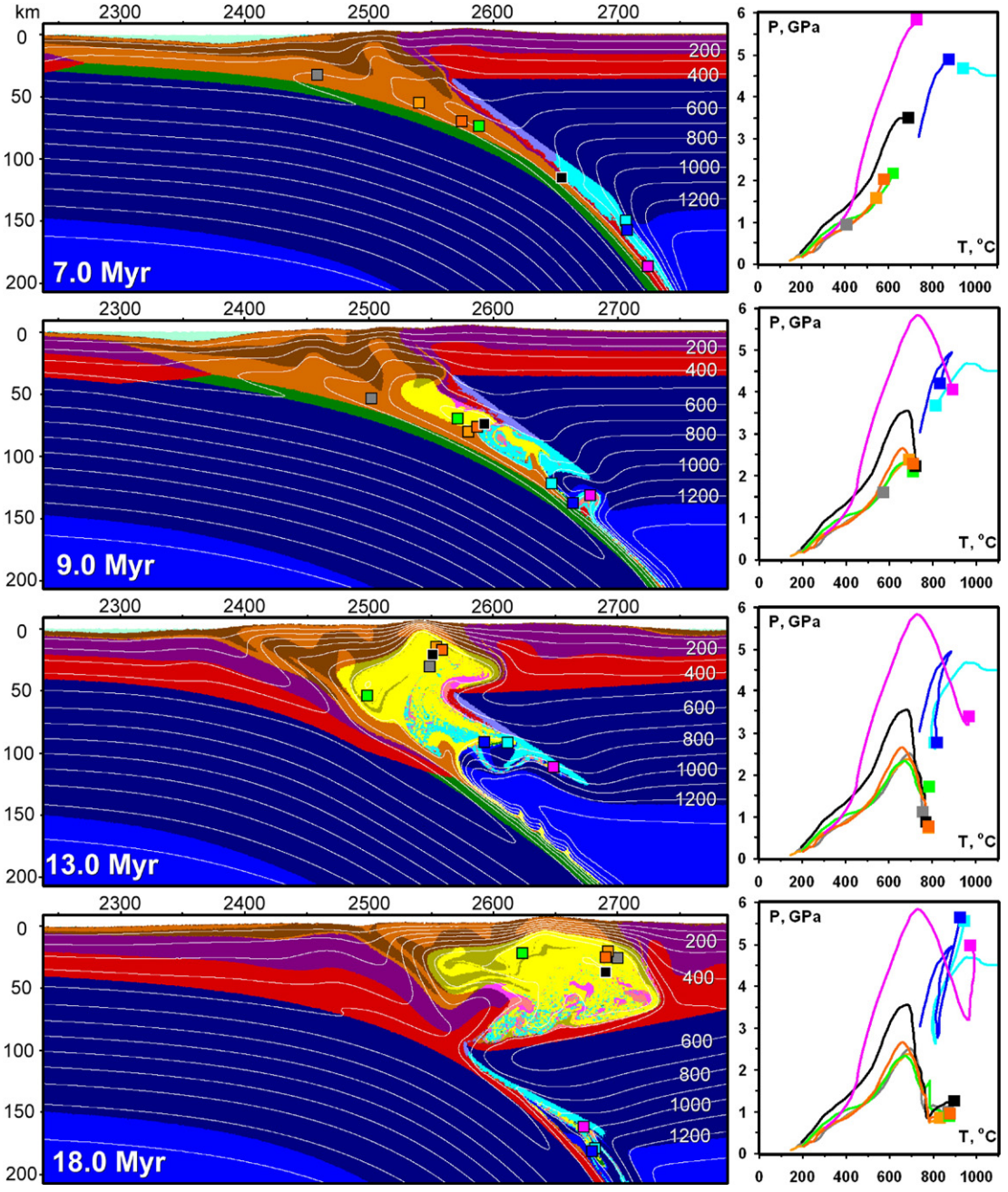

Fig. 9. Enlarged 550×210 km areas of the original 4000 km×670 km reference Model 16, with convergence rate=5 cm yr^{-1} and zero erosion rate (Table 3). Rock colors are as in Fig. 4. Time (Myr) of shortening is given in the figures. White numbered lines are isotherms in °C. Colored rectangles show positions of representative markers (rock units) for which P–T paths are shown. Initial positions of markers are shown in Fig. 2. As in Fig. 4, marker colors do not correspond to that of rock types. Vertical scale: depth below the z=8 km sea level.

temperatures as high as 1000–1100 °C. This mechanism would provide a voluminous source for syn-orogenic felsic magmatism. This model also shows repetitive loops in the *P–T* trajectories of some representative rock units (cf. pink marker in Fig. 8) with an HP–LT loop superimposed onto an earlier UHP–HT loop.

Variations in erosion rate significantly affect the tectonic style of incipient collision processes. Fig. 9 displays results from Model 16, which has zero erosion rate and other parameters identical to Model 1 shown in Fig. 4 (Table 3). These two models show similar geometry and *P–T* paths of identical markers at the beginning (<9 Myr) while later stages strongly differ due to slab delamination in the model without erosion. Model without erosion shows larger volume of thickened crust with higher and broader topography having only one major maximum located above UHP–HT complex (in contrast to two maxima for the model

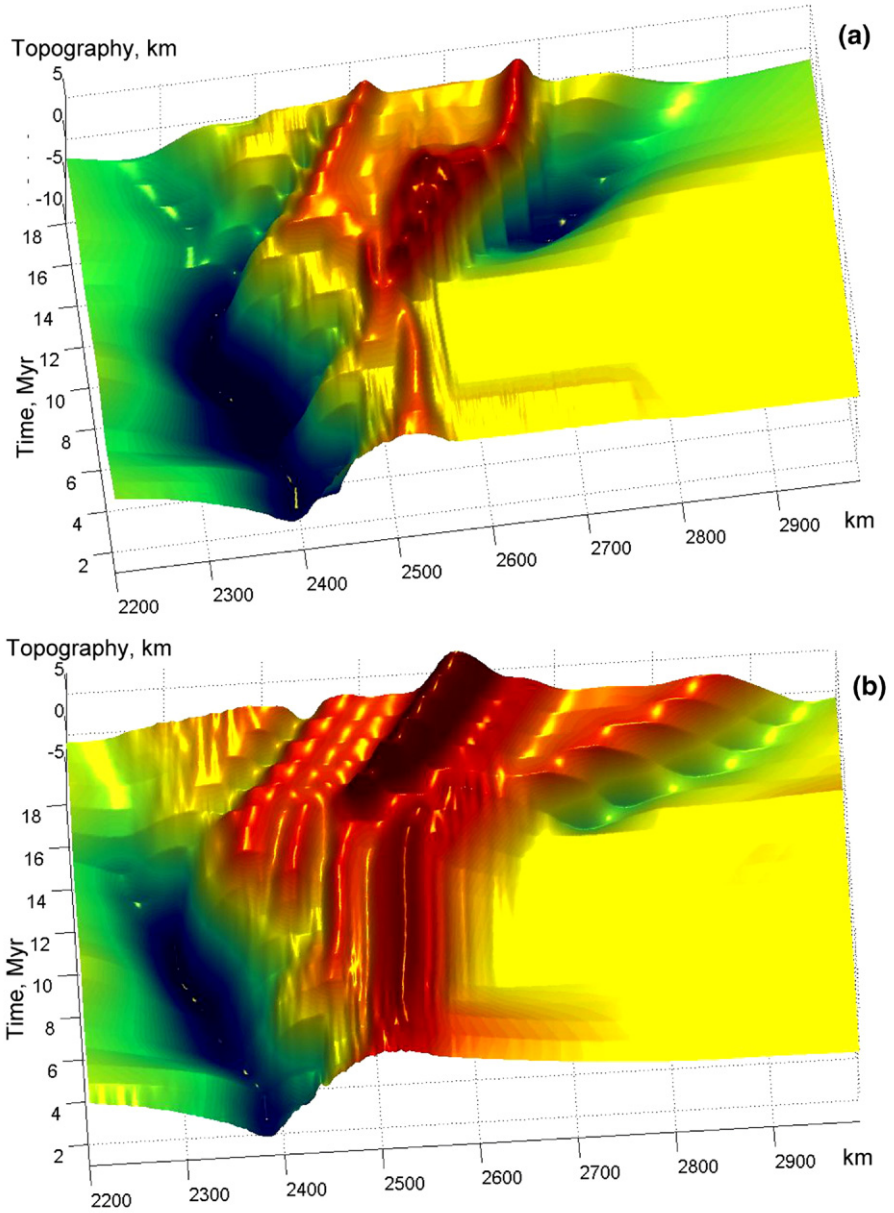

Fig. 10. Comparison of topography evolution for the model with (a, Model 1, Fig. 4, Table 3) and without (b, Model 16, Fig. 9, Table 3) erosion. Topography is computed with respect to $z=8$ km level.

with erosion, Fig. 10). Emplacement of UHP–HT rocks extruded from the hot channel is also very different — these rocks are broadening in the lower and middle crust and are not thrust over hanging wall rocks propagating toward the surface as in the models with erosion (cf. Figs. 4, 8, 9, 13–18 Myr).

4. Discussion

Numerical experiments demonstrate the transient character of the "hot channel effect", which operates at the transition from subduction to collision. The life span of the hot channel varies proportionally to the shortening rate: 15–20 Myr at 3 cm/yr (Model 3, Table 3), 8–12 Myr at 5 cm/yr (Model 1, Table 3), 4–7 Myr at 10 cm/yr (Model 4, Table 3). During this transition the physical conditions and evolution is comparable to those commonly inferred from UHP–HT rocks. The establishment of hot channels is primarily controlled by the intensity of viscous (Burg and Gerya 2005) and radioactive heating in subducted crustal rocks and seems to be less sensitive to other physical parameters such as erosion rate, density and rheology of rocks and shortening rate (Table 3). The hot tectonic channel becomes unstable at mature collision. Accordingly, peak metamorphism ages of UHP rocks will correspond to pre- to early-collisional stages. This is in agreement with published geochronology (e.g. Eide and Liou, 2000).

Our numerical results suggest that incipient collision is often associated with tectonic underplating of subducted crustal rocks beneath the overriding lithosphere and that later slab delamination is associated with the exhumation of rocks from the deep channel (Fig. 8). The same sequence of events has recently been documented by Boutelier et al. (2004) in thermo-mechanical, analog experiments that show strong similarity to the numerical models presented here. Ductile extrusion of rocks from a rheologically weak deep tectonic channel (Fig. 5a) has previously been obtained numerically by Burov et al. (2001), although their crustal channel was prescribed initially and not formed spontaneously as in this study. In additions, shear heating, partial melting, and P–T–time paths of rocks calculated here were not modeled.

An important issue related to the significance of UHP rocks refers to tectonic "overpressure", which characterizes the difference between mean stress (dynamic tectonic pressure) and the lithostatic pressure (e.g., Mancktelow, 1995; Petrini and Podladchikov, 2000; Burg and Gerya, 2005; Mancktelow, 2008-this volume). The comparison between these two pressure components computed along characteristic P–T paths of different material points from the reference Model 1 (Fig. 4) is illustrated in Fig. 11. Significant 10–40% deviations of the dynamic pressure from lithostatic values exist for relatively low pressures <2 GPa while dynamic and lithostatic pressures overlap for UHP conditions (Fig. 11b). This is also displayed by the spatial distribution of tectonic overpressure (Fig. 5c) in which the deep hot channel is characterized by insignificant (<5%) tectonic underpressure while up to 20% overpressure is reached in the colder and wider upper part of the channel. This result contrasts with the up to 20% overpressure computed for the lower portions of stable and closed subduction wedges (e.g., Fig. 8, 26.8 Myr) between two rigid plates (Mancktelow, 1995, 2008-this volume; Burg and Gerya, 2005). The difference is related to the transient nature of the hot channel which is open at depth and is stabilized by buoyancy. This configuration precludes large deviatoric stresses as well as over- and underpressures (Fig. 5c, d). However, high stresses and over/underpressures in the bending mantle lithosphere of both subducting and overriding plates (Fig. 5c,d) are consistent with previous results on more mature collision processes (Burg and Gerya, 2005).

Another important question concerns burial and exhumation rates of UHP rocks. As follows from Figs. 4 and 6, exhumation (decompression) rates within extruding hot channel are comparable or even up to 50% higher

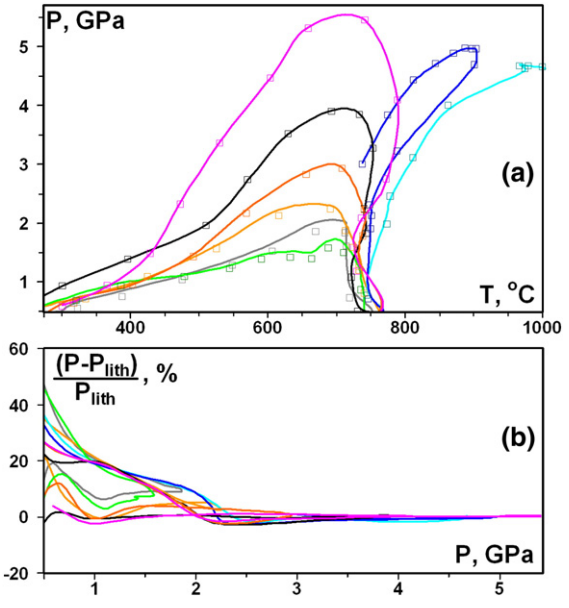

Fig. 11. Comparison between lithostatic pressure (open rectangles) and mean stress (dynamic tectonic pressure, solid lines) along P–T paths for representative markers (rock units) of Model 1 (Figs. 4, 5, Table 3). Positions of the markers are shown in Fig. 4.

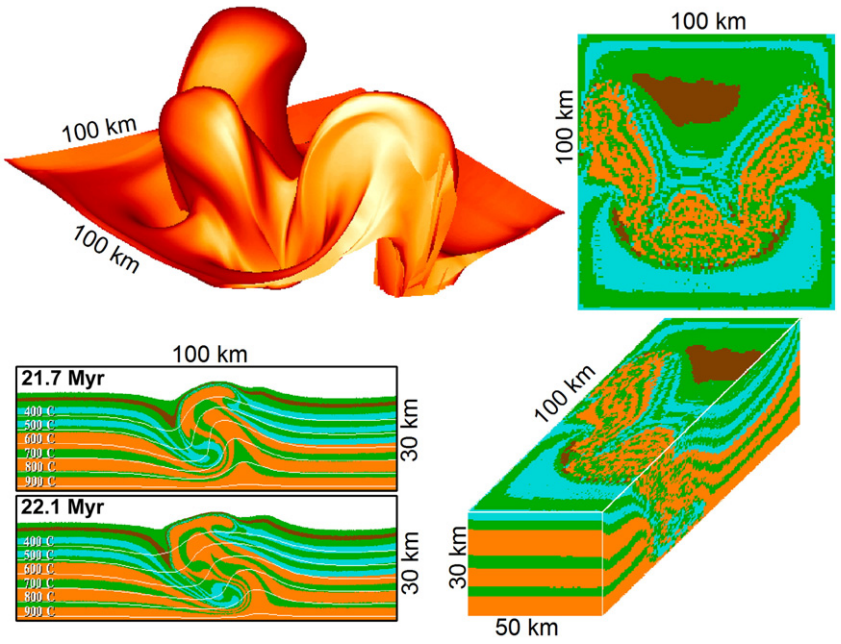

Fig. 12. Results of 3-D and 2-D numerical modeling (Gerya et al., 2000) for the growth of elongated granulitic (orange) cupola chains along the arc-like cratonic boundary due to the gravitational redistribution process in the inherently unstable hot continental crust (Perchuk, 1989; Gerya et al., 2004b).

than burial (pressurizing) rates. Typical decompression/exhumation rates (0.5–1.5 GPa/Myr, 1–5 cm/yr) are on the order of plate velocity and much faster than typical erosion rates imposed in the model (Table 3). It is therefore noteworthy that erosion plays a role close to the surface, for the terminal part of UHP rock histories only while major mechanisms of deep rock exhumation encompass forced circulation and buoyant ductile extrusion. Indeed, erosion can significantly affect tectonic styles of incipient collision and contribute to crustal strain localization (Ellis et al., 2001) and focusing exhumation flows (cf. Figs. 4, 8, 9, 13–18 Myr).

The geological pertinence of these model results is notable. UHP conditions precede collision, and are therefore relicts in collision orogens. This geochronological distinction has been emphasised in many UHP regions, sometimes leading to the conclusion that these regions are polyorogenic (Aleksandrowski et al., 2000). Old ages compared to the background orogenic age are generally reported from all UHP–LT regions (e.g. review of Liou and Zhang, 2004). These rocks are often overprinted by (U)HP–HT conditions that are a few million years younger (e.g. review by Ernst, 2001; Kröner et al., 2000). They occur in very thin nappe stacks (see reviews and e.g. Maruyama and Parkinson, 2000), which fits the mixing patterns developed in numerical experiments. UHP rocks suffer rapid decompression during pure shear deformation (e.g. Bröcker and Klemd, 1996) and extensional unroofing (e.g. Reinhardt and Kleemann, 1994). These features fit the rapid upward extrusion (regurgitation) along with thinning down to closure of the numerical hot channel. Associated molten rocks trigger gravitational instabilities that will favor the formation of domal structures (Fig. 12) as described in the Dabie Shan (e.g. Schmid et al., 2001) and the Himalayas (e.g. de Sigoyer et al., 2004). Development of domal and diapiric structures in collisional orogens is a characteristic feature when hot, partially molten, buoyant rocks are formed at the bottom of the continental crust (Figs. 4, 9, 12) causing its gravitational instability (e.g. Ramberg, 1981; Gerya et al., 2000, 2004b). Flattened geometry of these structures forming chains along the collision zone (Fig. 12) is related to the regional deformation under conditions of acting orogenic stresses.

5. Conclusions

The hot channel scenario implies a sequence of metamorphic events amenable to geological documentation: (1) (U)HP–LT conditions related to subduction progress toward (2) UHP–HT conditions during the formation of the hot tectonic channel at incipient collision; (3) temperature increase causes partial melting of subducted crustal

rocks under (U)HP condition and triggers (4) buoyant exhumation of channel rocks toward (5) HP–HT conditions typical for high pressure granulites (e.g., O'Brien, 2000) and further to (6) LP–HT conditions during the emplacement of the channel complex in the middle and upper crust. High temperature and strong positive buoyancy of partially molten rocks will yield doming and diapirism in the developing orogen (e.g., Ramberg, 1981; Gerya et al., 2004b; Burg and Gerya, 2005). Gravitational redistribution processes in the hot crust (Perchuk, 1989; Perchuk et al., 1992; Gerya et al., 2000, 2004b) will strongly contribute to the emplacement of elongated domal/diapiric cupola chains (Fig. 12). The systematically reproduced transient, hot channels with varying conditions is, along with fitting geological information, an encouragement to believe that the models are relevant to the early evolution of collisional systems. We emphasise that UHP metamorphic conditions are the transient signature of incipient processes, those that take place just before total collision between to converging continents. We are currently exploring direct application to the UHP and HP rocks found among large volumes of molten crustal rocks as in the Variscides and the Western Himalaya.

Acknowledgments

This work was supported by ETH Research Grants TH-12/04-1, TH-12/05-3, SNF Research Grant 200021-113672/1 and by the RF President Program "Leading Scientific School of Russia" (grant #03.5.1645 to LLP) and the RFBR grants # 03-05-64633 (to TVG) and #02-05-64025 (to LLP). Constructive reviews by S. Buiter and anonymous reviewer are greatly appreciated.

References

Aleksandrowski, P., Kryza, R., Mazur, S., Pin, C., Zalasiewicz, J.A., 2000. The Polish Sudetes: Caledonian or Variscan? Transactions Royal Soc. Edinburgh. Earth Sci. 90, 127–146.

Amato, J.M., Johnson, C.M., Baumgartner, L.P., Beard, B.L., 1999. Rapid exhumation of the Zermatt–Saas ophiolite deduced from high-precision Sm–Nd and Rb–Sr geochronology. Earth Planet. Sci. Lett. 171, 425–438.

Bakun-Czubarow, N., 1991. On the possibility of occurrence of quartz pseudomorphs after coesite in the eclogite–granulite rock series of the Złote Mountaind in the Sudetes (SW Poland). Arch. Mineral. XLVII (1), 6–13.

Bakun-Czubarow, N., 1998. Ilmenite-bearing eclogites of the West Sudetes — their geochemistry and mineral chemistry. Arch. Mineral. LI (1–2), 29–99.

Bittner, D., Schmeling, H., 1995. Numerical modeling of melting processes and induced diapirism in the lower crust. Geophys. J. Int. 123, 59–70.

Boutelier, D., Chemenda, A., Jorand, C., 2004. Continental subduction and exhumation of high-pressure rocks: insights from thermo-mechanical laboratory modeling. Earth Planet. Sci. Lett. 222, 209–216.

Bröcker, M., Klemd, R., 1996. Ultrahigh-pressure metamorphism in the Snieznik Mountains (Sudetes, Poland): *P–T* constraints and geological implications. J. Geol. 104, 417–433.

Brace, W.F., Kohlestedt, D.L., 1980. Limits on lithospheric stress imposed by laboratory experiments. J. Geophys. Res. 85, 6248–6252.

Burg, J.-P., Gerya, T.V., 2005. Viscous heating and thermal doming in orogenic metamorphism: numerical modeling and geological implications. J. Metamorph. Geol. 23, 75–95.

Burov, E., Jolivet, L., Le Pourhiet, L., Poliakov, A., 2001. A thermomechanical model of exhumation of high pressure (HP) and ultra-high pressure (UHP) metamorphic rocks in Alpine-type collision belts. Tectonophysics 342, 113–136.

Carswell, D.A., 1991. Variscan high *P–T* metamorphism and uplift history in the Moldanubian Zone of the Bohemian Massif in Lower Austria. Eur.J. Mineral. 3, 323–342.

Carswell, D.A., O'Brien, P., 1993. Thermobarometry and geotectonic significance of high-pressure granulites: examples from the Moldanubian zone of the Bohemian Massif in Lower Austria. J. Petrol. 343, 427–459.

Chemenda, A.I., Mattauer, M., Mattavieille, J., Bokun, A.N., 1995. A mechanism for syn-collisional rock exhumation and associated normal faulting: results from physical modelling. Earth Planet. Sci. Lett. 132, 225–232.

Chemenda, A., Burg, J.P., Mattauer, M., 2000. Evolutionary model of the Himalaya–Tibet system: geopoem based on new modelling, geological and geophysical data. Earth Planet. Sci. Lett. 174, 397–409.

Chopin, C., 1984. Coesite and pure pyrope in high-grade pelitic blueschists of the Western Alps: a first record and some consequences. Contrib. Mineral. Petrol. 86, 107–118.

Chopin, C., 2003. Ultrahigh-pressure metamorphism: tracing continental crust into the mantle. Earth Planet. Sci. Lett. 212, 1–14.

Clauser, C., Huenges, E., 1995. Thermal conductivity of rocks and minerals. In: Ahrens, T.J. (Ed.), Rock Physics and Phase Relations. American Geophysical Union, Washington, D.C., pp. 105–126. Reference Shelf 3.

de Sigoyer, J., Guillot, S., Dick, P., 2004. Exhumation of the ultrahigh-pressure Tso Morari unit in eastern Ladakh (NW Himalaya): a case study. Tectonics 23. doi:10.1029/2002TC00149.

Dobrzhinetskaya, L.F., Green II, H.W., Wang, S., 1996. Alpe Arami: a peridotite massif from depths of >300 km. Science 271, 1841–1845.

Eide, E.A., Liou, J.G., 2000. High-pressure blueschists and eclogites in Hong´an: a framework for addressing the evolution of high- and ultrahigh-pressure rocks in central China. Lithos 52, 1–22.

Ellis, S., Wissing, S., Beaumont, C., Pfiffner, A., 2001. Strain localisation as a key to reconciling experimentally derived flow-law data with dynamic models of continental collision. Int. J. Earth Sci. (Geol. Rundsch.) 90, 168–180.

Engi, M., Berger, A., Roselle, G.T., 2001. Role of the tectonic accretion channel in collisional orogeny. Geology 29, 1143–1146.

Ernst, W.G., 2001. Subduction, ultrahigh-pressure metamorphism, and regurgitation of buoyant crustal slices — implications for arcs and continental growth. Phys. Earth Planet. Inter. 127, 253–275.

Gerya, T.V., Yuen, D.A., 2003a. Characteristics-based marker-in-cell method with conservative finite-differences schemes for modeling geological flows with strongly variable transport properties. Phys. Earth Planet. Inter. 140, 293–318.

Gerya, T.V., Yuen, D.A., 2003b. Rayleigh–Taylor instabilities from hydration and melting propel "cold plumes" at subduction zones. Earth Planet. Sci. Lett. 212, 47–62.

Gerya, T.V., Stöckhert, B., 2006. 2-D numerical modeling of tectonic and metamorphic histories at active continental margins. Int. J. Earth Sci. (Geol. Rundsch.) 95, 250–274.

Gerya, T.V., Yuen, D.A., 2007. Robust characteristics method for modelling multiphase visco-elastoplastic thermo-mechanical problems. Phys. Earth Planet. Inter. doi:10.1016/j.pepi.2007.04.015.

Gerya, T.V., Perchuk, L.L., Van Reenen, D.D., Smit, C.A., 2000. Two-dimensional numerical modeling of pressure–temperature–time paths for the exhumation of some granulite facies terrains in the Precambrian. J. Geodyn. 30, 17–35.

Gerya, T.V., Stöckhert, B., Perchuk, A.L., 2002. Exhumation of high-pressure metamorphic rocks in a subduction channel — a numerical simulation. Tectonics 21, 6–1-6-19 Art. No. 1056.

Gerya, T.V., Yuen, D.A., Sevre, E.O.D., 2004a. Dynamical causes for incipient magma chambers above slabs. Geology 32, 89–92.

Gerya, T.V., Perchuk, L.L., Maresch, W.V., Willner, A.P., 2004b. Inherent gravitational instability of hot continental crust: implication for doming and diapirism in granulite facies terrains In: Whitney, D., Teyssier, C., Siddoway, C.S. (Eds.), Gneiss Domes in Orogeny. The Geological Society of America, Boulder, Colorado, pp. 97–115. Special Paper 380.

Gerya, T.V., Connolly, J.A.D., Yuen, D.A., Gorczyk, W., Capel, A.M., 2006. Seismic implications of mantle wedge plumes. Phys. Earth Planet. Inter. 156, 59–74.

Godard, G., Martin, S., Prosser, G., Kienast, J.R., Morten, L., 1996. Variscan migmatites, eclogites and garnet–peridotites of the Ulten zone, Eastern Austroalpine system. Tectonophys 259, 313–341.

Ito, K., Kennedy, G.C., 1967. Melting and phase relations in the basalt–peridotite system to 40 kbars. Am. J. Sci. 265, 519–542.

Klemd, R., Bröcker, M., 1999. Fluid influence on mineral reactions in ultrahigh-pressure granulites: a case study in the Sniezhnik Mts (West Sudetes, Poland). Contrib. Mineral. Petrol. 136, 358–373.

Kotkova, J., Harley, S.L., Fisera, M., 1997. A vestige of very high-pressure (ca. 28 kbar) metamorphism in the Variscan Bohemian Massif, Czech Republic. Eur. J. Mineral. 9, 1017–1033.

Kröner, A., O'Brien, P.J., Nemchin, A.A., Pidgeon, R.T., 2000. Zircon ages for high pressure granulites from South Bohemia, Czech Republic, and their connection to Carboniferous high temperature processes. Contrib. Mineral. Petrol. 138, 127–142.

Kryza, R., Pin, C., Vielzeuf, D., 1996. High-pressure granulites from the Sudetes (south–west Poland): evidence of crustal subduction and collisional thickening in the Variscan belt. J. Metamorph. Geol. 14, 531–546.

Liou, J.G., Zhang, R.-Y., 2004. Ultrahigh-pressure metamorphic rocks. Encycl. Phys. Sci. Technol. 227–244.

Mancktelow, N.S., 1995. Nonlithostatic pressure during sediment subduction and the development and exhumation of high pressure metamorphic rocks. J. Geophys. Res. 100, 571–583.

Mancktelow, N.S., 2008. Tectonic pressure: theoretical concepts and modelled examples. Lithos 103, 149–177 (this volume). doi:10.1016/j.lithos.2007.09.013.

Maruyama, S., Parkinson, C.D., 2000. Overview of the geology, petrology and tectonic framework of the HP/UHP metamorphic belt of the Kokchetav Massif, Kazakhstan. The Isl. Arc 9, 439–455.

Massonne, H.-J., 1999. A new occurrence of microdiamonds in quartzofeldspathic rocks of the Saxonian Erzgebirge, Germany, and their metamorphic evolution In: Gurney, J.J., Gurney, J.L., Pascoe, M. D., Richardson, S.H. (Eds.), The P.H. Nixon Volume Proceedings 7th International Kimberlite Conference, vol. 2. Cape Town, pp. 533–539.

Obata, M., Morten, L., 1987. Transformation of spinel lherzolite to garnet lherzolite in ultramafic lenses of the Austridic crystalline complex, northern Italy. J. Petrol. 28, 599–623.

O'Brien, P.J., 2000. The fundamental Variscan problem: high-temperature metamorphism at different depths and high-pressure metamorphism at different temperatures In: Franke, W., Haak, V., Onken, O., Tanner, D. (Eds.), Orogenic Processes: Quantification and Modelling In the Variscan Belt, 179. Geological Society, London, pp. 369–386. Special publications.

O'Brien, P.J., Kröner, A., Jaeckel, P., Hegner, E., Zelasniewicz, A., Krysza, R., 1997. Petrological and isotopic studies on Palaeozoic high pressure granulites, Gory Sowie Mts, Polish Sudetes. J. Petrol. 38, 433–456.

O'Hara, M.J., Richardson, S.W., Wilson, G., 1971. Garnet–peridotite stability and occurrence in earth and mantle. Contrib. Mineral. Petrol. 36, 48–68.

Peacock, S.M., 1987. Serpentinization and infiltration metasomatism in the Trinity peridotite, Klamath province, northern California: implications for subduction zones. Contrib. Mineral. Petrol. 95, 55–70.

Perchuk, L.L., 1989. *P–T*–fluid regimes of metamorphism and related magmatism with specific reference to the Baikal Lake granulites. In: Daly, S., Yardley, D.W.D., Cliff, B. (Eds.), Evolution of Metamorphic Belts. Spec. Publ. Geological Society, London, pp. 275–291.

Perchuk, L.L., Podladchikov, Y.Y., Polyakov, A.N., 1992. *P–T* paths and geodynamic modelling of some metamorphic processes. J. Metamorph. Geol. 10, 311–319.

Perchuk, L.L., Yapaskurt, V.O., Okay, A., 1995. Comparative petrology of diamond-bearing metamorphic complexes. Petrology 3 (3), 238–276.

Perchuk, A.L., Yapaskurt, V.O., Podlesskii, S.K., 1998. Genesis and exhumation dynamics of eclogites in the Kokchetav massif near mount Sulu-Tjube, Kazakhstan. Geochem. Int. 36, 877–885.

Perchuk, L.L., Tokarev, D.A., Parfenova, O.V., Podgornova, S.T., 2004. Metamorphic rocks of the Samerberg Complex, Eastern Alps: 1. petrography. Petrology 12 (2), 93–133.

Perchuk, L.L., Korchagina, M.A., Yapaskurt, V.O., Bakun-Czubarow, N., 2005. Some high-pressure metamorphic complexes in the west sudetes, Poland: I. petrography and mineral chemistry. Petrology 13 (5), 427–468.

Petrini, K., Podladchikov, Y., 2000. Lithospheric pressure–depth relationship in compressive regions of thickened crust. J. Metamorph. Geol. 18, 67–77.

Pinkerton, H., Stevenson, R.J., 1992. Methods of determining the rheological properties of magmas at subliquidus temperatures. J. Volcanol. Geotherm. Res. 53, 47–66.

Ramberg, H., 1981. Gravity, Deformation and Geological Application. Academic Press, New York. 452 p.

Ranalli, G., 1995. Rheology of the Earth, 2nd edition. Chapman and Hall, London. 413 p.

Reinhardt, J., Kleemann, U., 1994. Extensional unroofing of granulitic lower crust and related low-pressure, high-temperature metamorphism in the Saxonian Granulite Massif, Germany. Tectonophysics 238, 71–94.

Roermund, H.L.M., Drury, M.R., Barnhoorn, A., De Ronde, A.A., 2000. Super-silicic garnet microstructure from an orogenic garnet peridotites an ultra-deep (>6 GPa) origin. J. Metamorph. Geol. 18, 135–147.

Rosen, O.M., Zorin, Y.M., Zayachkovsky, A.A., 1972. A find of a diamond linked with eclogites of the Precambrian Kokchetav massif. Dokl. Akad. Nauk SSSR 203, 674–676 (in Russian).

Roselle, G.T., Engi, M., 2002. Ultra high pressure (UHP) terrains: lessons from thermal modeling. Am. J. Sci. 302, 410–441.

Rubatto, D., Hermann, J., 2001. Exhumation as fast as subduction. Geology 29, 3–6.

Schmid, R., Ryberg, T., Ratschbacher, L., Schulze, A., Franz, L., Oberhänsli, R., Dong, S., 2001. Crustal structure of the eastern Dabie Shan interpreted from deep reflection and shallow tomographic data. Tectonophysics 333, 347–359.

Schmidt, M.W., Poli, S., 1998. Experimentally based water budgets for dehydrating slabs and consequences for arc magma generation: Earth Planet. Sci. Lett. 163, 361–379.

Schreyer, W., 1988. Subduction of continental crust to mantle depths: petrological evidence. Episodes 11, 97–104.

Stöckhert, B., Gerya, T.V., 2005. Pre-collisional high pressure metamorphism and nappe tectonics at active continental margins: a numerical simulation. Terra Nova 17, 102–110.

Stöckhert, B., Duyster, J., Trepmann, C., Massonne, H.-J., 2001. Microdiamond daughter crystals precipitated from supercritical COH silicate fluids included in garnet, Erzgebirge, Germany. Geology 29, 391–394.

Tumiati, S., Thoni, M., Nimis, P., Martin, S., Mair, V., 2003. Mantle–crust interactions during Variscan subduction in the Eastern Alps (Nonsberg–Ulten zone): geochronology and new petrological constraints. Earth Planet. Sci. Lett. 210, 509–526.

Turcotte, D.L., Schubert, G., 1982. Geodynamics: Application of continuum physics to geological problems. John Wiley, New York. 450 p.

Vance, D., Bickle, M., Ivy-Ochs, S., Kubik, P.W., 2003. Erosion and exhumation in the Himalaya from cosmogenic isotope inventories of river sediments. Earth Planet. Sci. Lett. 206, 273–288.

Willner, A.P., Rötzler, K., Maresch, W.V., 1997. Pressure–temperature and fluid evolution of quartzo-feldspathic metamorphic rocks with a relic high-pressure, granulite-facies history from the Central Erzgebirge (Saxony, Germany). J. Petrol. 38, 307–336.